pubs.acs.org/Biomac

Article

Synergistic Effect of Physical and Chemical Cross-Linkers Enhances Shape Fidelity and Mechanical Properties of 3D Printable Low-Modulus Polyesters

Deliris N. Ortiz-Ortiz, Abdol Hadi Mokarizadeh, Maddison Segal, Francis Dang, Mahdi Zafari, Mesfin Tsige, and Abraham Joy*

Cite This: *Biomacromolecules* 2023, 24, 5091−5104

Read Online

ACCESS | Metrics & More | Article Recommendations | Supporting Information

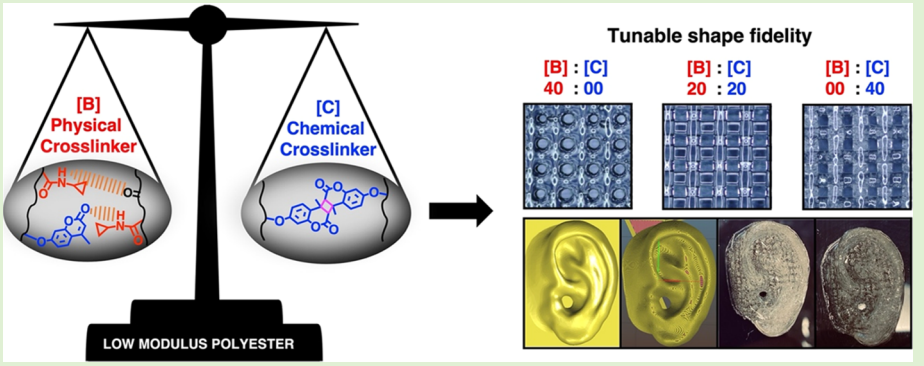

ABSTRACT: Three-dimensional (3D) printing is becoming increasingly prevalent in tissue engineering, driving the demand for low-modulus, high-performance, biodegradable, and biocompatible polymers. Extrusion-based direct-write (EDW) 3D printing enables printing and customization of low-modulus materials, ranging from cell-free printing to cell-laden bioinks that closely resemble natural tissue. While EDW holds promise, the requirement for soft materials with excellent printability and shape fidelity postprinting remains unmet. The development of new synthetic materials for 3D printing applications has been relatively slow, and only a small polymer library is available for tissue engineering applications. Furthermore, most of these polymers require high temperature (FDM) or additives and solvents (DLP/SLA) to enable printability. In this study, we present low-modulus 3D printable polyester inks that enable low-temperature printing without the need for solvents or additives. To maintain shape fidelity, we incorporate physical and chemical cross-linkers. These 3D printable polyester inks contain pendant amide groups as the physical cross-linker and coumarin pendant groups as the photochemical cross-linker. Molecular dynamics simulations further confirm the presence of physical interactions between different pendants, including hydrogen bonding and hydrophobic interactions. The combination of the two types of cross-linkers enhances the zero-shear viscosity and hence provides good printability and shape fidelity.

1. INTRODUCTION

There is a pressing demand for the development of synthetic three-dimensional (3D) printable materials with the modulus of native tissues and the ability to accurately replicate the anatomical details and biological characteristics of organs. These materials should possess characteristics such as elasticity, self-healing, tunable degradability, soft mechanical properties, and a porous structure. In addition, their properties and behavior need to be properly studied and understood. 3D printing has the potential to be used for fabricating complex structures with intricate architecture, thereby providing an alternative avenue for patients waiting for organ transplants. In 2022, the United States national transplant list,[1] as reported by the U.S Department of Health & Human Services, consisted of 103,544 patients. Strikingly, only 41,199 of these patients were fortunate enough to receive a transplant. This staggering disparity emphasizes the urgent need for innovative solutions, and 3D printing offers a promising alternative, which could significantly alleviate the burden on organ transplant waitlists. Although a functional synthetic organ is immensely more complex than a simplistic 3D printed scaffold, the design of materials with the appropriate physical and biochemical

Received: July 11, 2023
Revised: September 29, 2023
Published: October 26, 2023

properties is the first necessary step to achieve such functionally complex organs.

Several 3D printing techniques such as extrusion-based direct-write (EDW) 3D printing, fused deposition modeling (FDM), inkjet printing (IP), and stereolithography (SLA) have been explored to design complex biological structures.[2−10] However, these techniques face similar limitations.[11−15] The most common materials used for 3D printing can be categorized into two groups: natural and synthetic polymers. Natural polymers often exhibit batch-to-batch variability, poor mechanical properties, and poor shape fidelity.[16−21] On the other hand, synthetic polymers offer improved mechanical properties and shape fidelity,[22] making them suitable for applications such as tracheal splints,[23] bone cancer metastasis studies,[24] dental implants,[25] ear implants,[26] stents,[27,28] and orthopedic implants.[29,30] Unfortunately, synthetic polymers also come with their own drawbacks.[31,32] For instance, they can induce inflammation (poly(lactic-*co*-glycolic acid)),[33] bone erosion after years of device implantation (poly(tetrafluoroethylene)),[34,35] systemic and local reactions due to acidic byproducts (poly(lactic acid) and poly(lactic-*co*-glycolic acid)),[33,,37] poor cell adhesion due to hydrophobic characteristics (polycaprolactone),[38] and poor mechanical properties due to low elasticity and flexibility (polyetheretherketone and poly(lactic acid)).[38,39]

We have previously reported the design, synthesis, and characterization of a library of modular, multifunctional polyesters with pendant functional groups that mimic peptide side chains.[40] Polyesters from this modular library were used for solvent-free and room-temperature EDW 3D printing.[41−46] They display a predominantly viscous nature at room temperature with shear-thinning properties. Ultraviolet (UV) irradiation of coumarin-containing viscous inks converts them into elastomeric solids upon [2 + 2] photocycloaddition of the pendant coumarin unit.[47,48] However, the dependence on coumarin for achieving the fidelity of printed structures limited the compositions of the scaffolds and the types of active agents that can be incorporated into the scaffolds. Designing solvent-free, low-modulus, and soft bioinks with high shape fidelity is challenging, as these two properties are oppositely correlated.[49,50] A strategy for achieving good shape fidelity of 3D structures while balancing polymer melt flow and shape fidelity is the incorporation of polymers reinforced through supramolecular forces such as hydrogen bonding. These reinforced polymers exhibit desirable characteristics such as viscosity modulation,[51] self-assembly,[52−54] self-healing,[55−58] adhesion,[57−59] and reversible properties.[60] Hydrogen bonds act as dynamic cross-links, enabling printing upon shear, while strengthening the material and reducing chain mobility postprinting through reorganization of the hydrogen bonds upon removal of the shear forces.[61,62] Moreover, hydrogen bonding containing secondary amide groups has been shown to create flexible chains that can switch easily between conformations due to their large bond angles. Our previous work has demonstrated that incorporating hydrogen bonds in low-modulus polyesters improves shape fidelity, while maintaining low-temperature printability.[63] In this work, we build upon our previous work and demonstrate that the polyesters designed here can be printed at ambient temperatures while exhibiting sufficient zero-shear viscosity to produce scaffolds with high shape fidelity.

In this work, we synthesized five different polyester compositions using carbodiimide-mediated step-growth polymerization of three N-functionalized monomers and studied their physical, chemical, and mechanical responses. These monomers include an alanine-mimicking monomer [**A**] to provide low-modulus polyesters, a diol [**B**] that contributes to physical cross-linking through hydrogen bonding, and a coumarin diol [**C**] that enables chemical cross-linking through UV-mediated [2 + 2] cycloaddition. Their rheological properties were analyzed to study their effect on the compositions. Under steady-state flow conditions, we examined the viscosity of the polymers as a function of the shear rate. Additionally, we employed small amplitude oscillatory shear rheology to evaluate the impact of the combination of physical and chemical cross-linkers on the viscoelastic properties. The 3D printability and shape fidelity of the polyesters were assessed based on their ability to extrude as a simple 2-layer structure, retain the printed geometry, and measure the changes in pore size before and after cross-linking. We also analyzed the relationships between printing pressure, flow speed, and the line weight of 3D printed constructs for each polyester. Molecular dynamics simulations were carried out to understand the inter- and intramolecular interactions of the polymers. Degradation and cytotoxicity studies provided information about polymer degradability and biocompatibility properties. These analyses provide valuable insights into the overall performance and suitability of polyesters for biomedical applications.

2. EXPERIMENTAL SECTION

2.1. Materials. All chemicals were used as received from the manufacturer unless otherwise indicated. Chemical synthesis reagents included sodium sulfate anhydrous (99.32%, Chem-Impex), 18-crown-6-ether (99%, Chem-Impex), 4-dimethylaminopyridine (99.38%, Chem-Impex), 4-toluenesulfonyl chloride (99.68%, Chem-Impex), *N*,*N*′-diisopropylcarbodiimide (DIC, 99.5%, Chem-Impex), sodium bicarbonate, triethylamine (>99.5%, VWR Chemicals), cyclopropylamine (VWR Chemicals), ethyl propionate (>99%, Acros Organics), sodium methoxide (>96%, TCI America), 4-methylumbelliferone (>98%, TCI America), succinic acid (>99%, TCI America), thionyl chloride (98%, TCI America), ethyl-8-bromooctanoate (>97%, Matrix Scientific), ethyl 4-bromobutyrate (98%, Thermo Fisher Scientific), sulfuric acid (Thermo Fisher Scientific), diethanolamine (>98%, Sigma-Aldrich), and *N*,*N*-bis(2-hydroxyethyl)-4-((4-methyl-2-oxo-2H-chromen-7-yl)oxy)butanamide (Cou, prepared according to literature[41]). Methanol (MeOH, Thermo Fisher Scientific), tetrahydrofuran (THF, Thermo Fisher Scientific), and dichloromethane (DCM, Thermo Fisher Scientific) were dried via distillation over anhydrous CaH_2. Silica gel (40−63 μm, 230 × 400 mesh, Sorbent Technologies Inc.). 4-(Dimethylamino)pyridinium-4-toluenesulfonate (DPTS, prepared according to literature[43]). Spectra/Por Dialysis Membranes (M_w CO: 3.5 kDa, Thomas Scientific). Sodium phosphonic acid (20 mM and pH 2.5) was prepared by using sodium dihydrogen phosphate monohydrated (10 mmol), phosphonic acid (85%, 10 mmol), and ultrapure water. Phosphate-buffered saline (PBS, 10×, Thermo Fisher Scientific).

2.2. Synthesis of Monomers and Copolyesters. In general, each diol monomer was synthesized by amidation of diethanolamine with the corresponding methyl ester of each desired pendant groups. The alanine monomer [**A**] was synthesized by the reaction of diethanolamine (2 equiv, 394.73 mmol) with ethyl propionate (1 equiv, 197.37 mmol). The reaction proceeded at 80 °C under stirring for 24 h. The cyclopropyl monomer [**B**] was synthesized by the reaction of cyclopropylamine (1 equiv, 184.86 mmol) with ethyl succinyl chloride (1 equiv, 181.24 mmol) in dry DCM. Then, the reaction flask was cooled to 0 °C and triethylamine (1 equiv, 184.86 mmol) was added. After 24 h, the reaction was washed with acidified water, extracted with DCM, and the organic layer was collected and

https://doi.org/10.1021/acs.biomac.3c00684
Biomacromolecules 2023, 24, 5091−5104

Table 1. Summary of Polyester Molar Ratio Composition, Molecular Mass, and Thermal and Physical Properties of Synthesized Polyesters

polymer	theoretical [A]/[B]/[C]	experimental [A]/[B]/[C]	M_n (kDa)	M_w (kDa)	$Đ$	T_g (°C)	T_d (°C)	η_0 (Pa·s)
$\mathbf{P_1}$	60:40:00	61:39:00	14.5	25.6	1.77	13.7	280.8	165.2
$\mathbf{P_2}$	60:35:05	61:35:04	12.9	22.7	1.76	16.2	280.8	944.8
$\mathbf{P_3}$	60:20:20	63:18:19	16.0	29.7	1.86	13.5	292.7	572.1
$\mathbf{P_4}$	60:05:35	60:08:32	16.4	26.0	1.63	13.3	297.1	518.6
$\mathbf{P_5}$	60:00:40	64:00:36	16.7	29.3	1.76	13.2	300.0	337.7

dried under high vacuum for 12 h to yield a yellow powder. Finally, the ethyl 4-(cyclopropylamino)-4-oxobutanoate product was then reacted with diethanolamine (2 equiv, 284.86 mmol) and sodium methoxide (0.05 equiv, 14.28 mmol) at 85 °C for 24 h under vacuum. The coumarin monomer [**C**] was obtained as follows: 7-hydroxy-4-methylcoumarin (1 equiv, 49.76 mmol) was taken in 90 mL of dry tetrahydrofuran. Then, potassium carbonate (2 equiv, 99.5 mmol), ethyl-8-bromooctanoate (2 equiv, 99.5 mmol), and 18-crown-6 (0.05 equiv, 2.50 mmol) were added, and the reaction was heated to 50 °C. The reaction mixture was stirred for 48 h at 50 °C, then extracted by using a 1:1 mixture of DCM/H_2O, filtered, concentrated, and dried under high vacuum for 24 h to yield a white product. This product (1 equiv, 18.53 mmol) was reacted with diethanolamine (2 equiv, 37.06 mmol) and sodium methoxide (0.05 equiv, 0.09 mmol) at 90 °C for 24 h. After completion of the final amidation step, each monomer was purified by column chromatography (DCM:MeOH, 9:1) to yield the monomer.

The copolyesters were synthesized by carbodiimide-mediated step-growth polymerization of three N-functionalized monomers. The diol monomer (1 equiv, mmol) (feed ratio shown in Table 1), succinic acid (1 equiv, 34.76 mmol), and 4-(dimethylamino)pyridinium-4-toluenesulfonate (DPTS) (0.4 equiv, 13.90 mmol) were mixed in a round-bottom flask equipped with an addition funnel. The reaction flask was connected to a Schlenk line and vacuum backfilled 3 times with N_2. Then, dried DCM (70 mL) was added to dissolve the reagents. The reaction was cooled in an ice bath to 0 °C before dropwise addition of DIC (3 equiv, 164.28 mmol). The reaction mixture was left to stir at room temperature for 48 h. Each polymer was purified by dialysis (M_w CO 3.5 kDa) with methanol and then precipitated in ether and dried under vacuum for 24 h to yield the desired polyester.

2.3. Copolyester Chemical and Morphological Characterization. The monomer and polymer structures and compositions were characterized by ^{1}H nuclear magnetic resonance (^{1}H NMR; 300 MHz Varian Mercury spectrophotometer) in DMSO-d_6. Chemical shifts (δ) of polymers and monomers were recorded in parts per million relative to the solvent signal at 2.5 ppm. Gel permeation chromatography (GPC) analysis was performed on two TSK-GEL Super H 3000 columns and one TSK-GEL Super H 4000 column in series and analyzed using a TOSOH Eco SEC HLC-8320 instrument. Samples were dissolved in DMF with a constant flow rate of 0.800 mL/min, and the number-average molecular weight (M_n) and weight-average molecular weight (M_w) were determined by referencing to polystyrene standards. Differential scanning calorimetry (DSC) characterization was performed to determine the glass transition temperature (T_g) of the polymers. The instrument was calibrated with an empty hermetic aluminum pan standard at 10 °C/min. Each sample was sealed in hermetic aluminum pans and the T_g of the samples were determined by ramping the sample from 0 to 200 °C with a scan rate of 10 °C/min, then holding them at 200 °C for 2 min and then ramping to −50 °C at 10 °C/min under a N_2 atmosphere. The heating and cooling processes were repeated 3 times. Thermogravimetric analysis (TGA) using a TA Q500 instrument at a heating rate of 10 °C/min from 0 to 800 °C in a N_2 atmosphere was used to obtain the thermal decomposition temperature (T_d) of the polymers.

2.4. Thermal Response of Hydrogen Bonding Molecules. Temperature dependence of IR absorption characterization (FT-IR) was performed to study the extent of hydrogen bonding. FT-IR samples were prepared by casting a thin film of polymers on potassium bromide (KBr) pellets from a 5% (w/w) polymer solution (DCM was used for $\mathbf{P_1}$−$\mathbf{P_5}$). The samples were kept under a high vacuum oven at 70 °C for 2 h to remove the residual solvent and moisture. An FT-IR spectrophotometer (Thermo Nicolet 380) with a temperature chamber was used to monitor the change of the spectra over temperature. The temperature was raised from 42 to 222 °C with an interval of 20 °C, and samples were kept isothermal for 3 min at each temperature before testing. 32 scans and a resolution of 2 cm^{-1} was used in the test. Peak fitting of the "bonded" and "free" N−H stretching peaks was done with Origin Pro 9.0. All spectra were normalized against the asymmetric C−H stretching peak (~2964 cm^{-1}) whose intensity did not change with increase of temperature.

2.5. Rheological Properties. Rheological characterization was performed on an ARES G2 rotational rheometer using 25 mm parallel plate geometry for a frequency sweep test and on a DHR2 25 mm cone and plate geometry for the shear rate sweep test. The polymer was loaded on the rheometer plate as a melt and heated to a temperature of T_g + 50 °C for 10 min to remove any residual stress before being equilibrated to the experimental temperature for another 10 min. The steady-state flow sweep was performed with a shear rate from 0.01−1.0 s^{-1}, and data was plotted as steady shear viscosity vs shear rate. Before the frequency sweep, strain sweeps with an angular frequency of 1 rad/s were run for each polymer at a specific temperature to determine the linear regime. The frequency sweep was performed on each polymer at 65 °C to obtain the storage modulus (G') and loss modulus (G'') vs frequency. $\mathbf{P_1}$ and $\mathbf{P_5}$ were soft at room temperature; this facilitated the handling of the polymers. They were loaded and studied with a temperature range between 25 and 140 °C. However, $\mathbf{P_2}$, $\mathbf{P_3}$, and $\mathbf{P_4}$ were heated up to 55−60 °C to be loaded due to low viscosity at room temperatures. To study the effects of physical and chemical cross-linkers, rheology studies to UV cross-linked polymer films with different cross-linking times were carried out. The films were fabricated by the solvent casting technique. The polymer melt was poured into a stainless-steel mold with a diameter of 10 mm and thickness of 1 mm and the mold was covered with two Teflon sheets on both sides. The mold was then kept in vacuum at 80 °C for 2 h under the pressure of a stainless-steel plate (1.2 kg, 152 mm × 152 mm × 6 mm) and cooled to room temperature. To safely remove the films from the mold, the mold was immersed in liquid nitrogen and both Teflon sheets were peeled off. The polymer films were then UV-irradiated by using an Omni Cure UV lamp with a wavelength range of 320−500 nm for different lengths of time (5, 10, 20, and 30 min each side) (I = 80 mW/cm^2). The G' and G'' values were plotted against the UV-irradiation time.

2.6. Mechanical Properties. Mechanical characterization was performed on UV cross-linked dog bone-shaped films. The preparation of UV cross-linked polymer films is similar to that in Section 2.5. A stainless-steel mold with dimensions of 3.0 × 2.0 × 0.5 mm^3 was used. Both sides of the polymer in the mold were UV-irradiated for 30 min. Dumbbell-shaped specimens were prepared by cutting the cross-linked polymer films using a die with half the size of the type V specimen according to ASTM D 638−03.73. The mechanical test was performed on an Instron 5530 (100 kN) with a crosshead speed of 0.5 mm/s until the specimen fractured. The engineering stress−strain curve for each polymer was recorded. In addition, the elastic modulus and strain at break were calculated based on the results from three samples.

https://doi.org/10.1021/acs.biomac.3c00684
Biomacromolecules 2023, 24, 5091−5104

Scheme 1. Chemical Structure and Molecular Compositions of the Statistical Copolyesters Used in this Study[a]

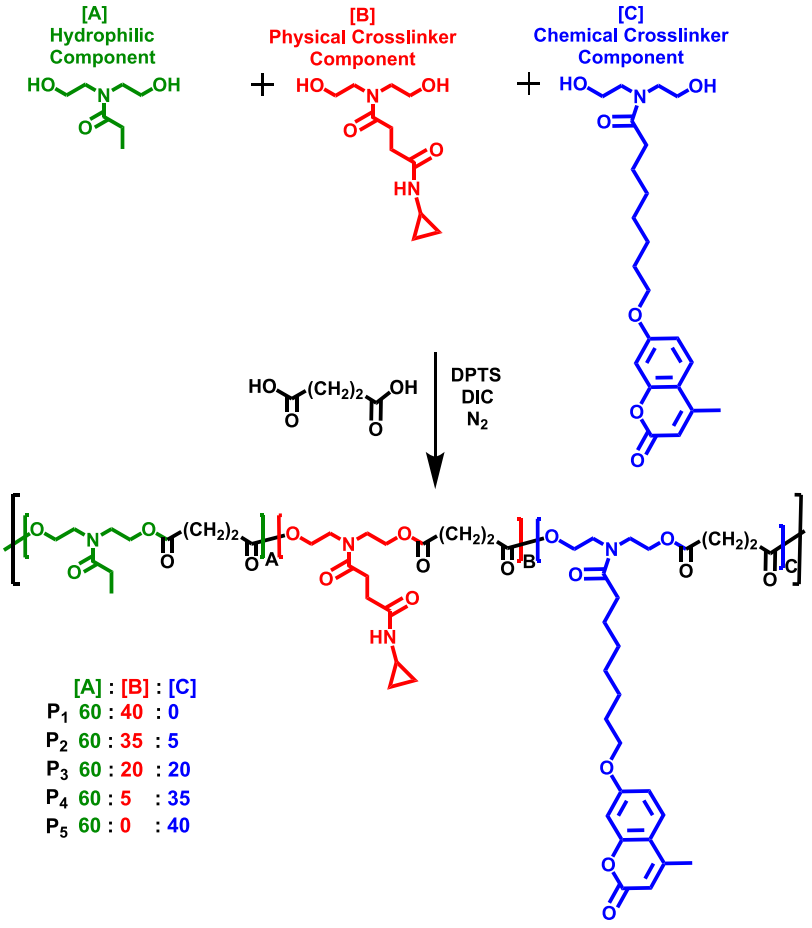

[a][A], [B], and [C] indicate the mol % of the three components in the polyesters P_1, P_2, P_3, P_4, and P_5.

2.7. 3D Printing and Shape Fidelity Assessment. The polyesters were printed via extrusion-based direct-write (EDW) 3D printing, where pneumatic pressure was applied to extrude continuous polymer filaments to form a layer-by-layer 3D construct. The printed architecture consisted of two-layered polymer scaffolds with a 0/90° crosshatch pattern. The polymer melt was loaded without any solvent or additives, and scaffolds were printed at 65 °C with a pressure of 150 kPa and a printing speed of 50 mm/sec. For the shape fidelity studies, we studied the ability of the scaffolds to hold the shape over time. The first study involved two-layered scaffolds and the observation of their pore shape change over time. Pictures of cross-linked and uncross-linked two-layered scaffolds were taken every 10 min over a 1 h period, and their shape fidelity was quantified using ImageJ. The shape descriptor parameters "circularity" and "printability" were used. Circularity or $C_r = \frac{4\pi A}{P^2}$ (where A is the area of the pore and P is the perimeter) describes the tendency of the extruded filament to exhibit a viscous state, leading to the pores between the crosshatch patterns transitioning from the expected square patterns to circular patterns. Printability or $P_r = \frac{\pi}{4C_r}$ is the ability to form 3D structures with good fidelity and integrity (where C_r is circularity).[63] Systems with high shape fidelity show a uniform line width, $C_r < 1$ and $P_r = 1$, while those with low shape fidelity show a nonuniform line width, $C_r = 1$ and $P_r < 1$. For C_r and P_r calculations, three scaffolds per composition were analyzed by ImageJ and the area of 6 non-consecutive pores was averaged. For the second study, the polymer that exhibited the highest printability values was selected to print an ear with size 34.55 × 32.05 × 8.70 mm^3, without any printing support for the overhang structures. This complex geometry involved printing more than 100 lines and hanging layers.

2.8. Degradation Study. The printed scaffolds were placed in a glass vial containing 2 mL of PBS and kept at physiological conditions (pH 7.4 and 37 °C). After 30 days, each film was washed with DI water, frozen with liquid nitrogen, and dried overnight in a lyophilizer. Then, the mass loss of the films was evaluated by measuring the weight of the films before and after freeze-drying and the weight change (ΔW) was calculated using eq 1

$$\Delta W = \left(\frac{W_0 - W_i}{W_0}\right) \times 100 \tag{1}$$

where W_0 is the initial polymer weight, and W_i is the final polymer weight (after overnight lyophilization).

2.9. Swelling Analysis. Scaffolds were prepared as previously described in Section 2.7. The 3D printed scaffolds were placed in a glass vial containing 2 mL of PBS and kept at physiological conditions (pH 7.4 and 37 °C). The samples were periodically removed from the incubator, water was removed, and excess water was patted dry. Then, the samples were weighed, and the percentage of swelling was calculated by using eq 2

$$\%\text{swelling} = \left(\frac{W_s - W_i}{W_i}\right) \times 100 \tag{2}$$

where W_s is the weight of the swollen scaffold, and W_i is the initial scaffold weight (before wetting).

2.10. 3D Printed Scaffold In Vitro Cytotoxicity via Lactate Dehydrogenase (LDH) Activity Assay. 3D printed scaffold cytotoxicity was measured via the Pierce LDH Cytotoxicity Assay Kit from Thermo Scientific. 3D printed scaffolds were first allowed to leach in DMEM supplemented with 10% FBS (D10 media) for 96 h,

https://doi.org/10.1021/acs.biomac.3c00684
Biomacromolecules 2023, 24, 5091−5104

where the supernatant was collected and replenished every 24 h. 200 μL of approximately 25,000 cells/mL of primary human dermal fibroblasts (HDFs) in D10 media was seeded into each well of a 96-well tissue-culture plate using 0.25% trypsin-EDTA. After incubation at 37 °C for 24 h, the media was removed and replaced with a scaffold-leached supernatant and incubated again at 37 °C for 24 h. Using the Invitrogen CyQUANT LDH Cytotoxicity Assay, a triplicate of untreated wells was lysed with the provided 10× lysis buffer and incubated at 37 °C for 40 min. 50 μL was then taken from each sample well and pipetted into a clear, 96-well flat-bottom plate. 50 μL of LDH Reaction Mix was then added to each well, mixed by gently tapping on the side of the well plate, and incubated in the dark at room temperature for 30 min. The plate was then read at 490 and 680 nm. To determine LDH activity, the 680 nm absorbance value (background) was subtracted from the 490 nm absorbance value before the calculation of % cytotoxicity, which was calculated from eq 3

$$\%\text{cytotoxicity} = \left[\frac{\text{C-T. LDH activity} - \text{S . LDH activity}}{\text{maximum LDH activity} - \text{S. LDH activity}}\right] \times 100 \quad (3)$$

where C-T. LDH activity is compound-treated LDH activity, and S. LDH activity is spontaneous LDH activity.

3. RESULTS AND DISCUSSION

3.1. Synthesis and Characterization of the Polyesters. We synthesized five polyesters ($\mathbf{P_1}$, $\mathbf{P_2}$, $\mathbf{P_3}$, $\mathbf{P_4}$, and $\mathbf{P_5}$) through carbodiimide-mediated step-growth polymerization of three N-functional monomers, each serving a specific purpose in the polymer properties. The first monomer [**A**], which mimics alanine, was incorporated to maintain a low modulus. The second monomer [**B**] contributed to physical cross-linking through hydrogen bonding. Finally, the third monomer [**C**], a coumarin diol, facilitated chemical cross-linking through a UV-mediated [2 + 2] cycloaddition reaction (Scheme 1). Table 1 presents the molar percentages of [**B**] and [**C**] components, with all polymers containing a fixed 60% molar ratio of monomer [**A**]. The variation in the amounts of [**B**] and [**C**] allowed us to investigate the impact of physical and chemical cross-linkers on the shape fidelity of the 3D printed scaffolds and their physical and mechanical response. ^{1}H NMR peak positions and integrations of monomers are depicted in Figure S1. Copolyester peak integration and monomer ratio calculations are depicted in Figure S2 and Table S1, respectively.

3.2. Molecular Characterization of Polyester Inks. The rheological properties, printability, and print quality of polymers can be influenced by differences in molecular weight, which in turn affect transition temperatures, viscosity, and mechanical properties. To minimize this effect, only the batches with M_w values from 22−29 kDa were used for this study. Table 1 provides the number-average molecular weight (M_n), weight-average molecular weight (M_w), glass transition temperature (T_g), decomposition temperature (T_d), and zero-shear viscosity (η_0) of each polyester. All characterizations were performed below the thermal decomposition temperature (T_d) to avoid chemical degradation. Molar mass distribution (dispersity, $Đ$) of the polymers was >1.5, which is lower than the theoretical value for step-growth polymerization ($Đ \sim 2$) due to purification steps prior to final characterization. Similar glass transition temperatures were observed for all of the polymer compositions. All five-polymer compositions showed very low T_g, which enables them to be printed at temperatures close to room temperature, as shown in Figure S7.

3.3. Variable-Temperature IR Absorption Spectroscopy. Variable-temperature Fourier-transform infrared (VT-FTIR) spectroscopy was used to understand the physical cross-linking in $\mathbf{P_1}$, $\mathbf{P_2}$, $\mathbf{P_3}$, $\mathbf{P_4}$, and $\mathbf{P_5}$. The analysis revealed the dynamic characteristics of hydrogen bonds in response to thermal stimuli from 42 to 222 °C. All spectra were normalized against the asymmetric C−H stretching peak at 2964 cm^{-1} (**band 4**), the intensity of which did not change with increasing temperature. Since the polymers are hygroscopic, prior to VT-FTIR characterization, the samples were dried overnight at 80 °C under high vacuum. The absorption **band 1** around 3593 cm^{-1} corresponding to the symmetric OH stretch of water shows the presence of residual water after drying in all samples.[64] The drastic decrease of this band on heating from 42 to 62 °C may be attributed to fast water evaporation from the surface of the film and slower evaporation from intermolecularly bonded water at much higher temperatures. The water percentage removal after heating the sample up to 222 °C for polymers $\mathbf{P_1}$−$\mathbf{P_5}$ was calculated to be 67, 71, 57, 53, and 46%, respectively. It can be assumed that minimal hydrogen bonding interactions due to water are present in all polymer samples for temperatures above 82 °C.

To investigate the presence of physical cross-linking in all polymers, we monitored changes in the infrared spectrum of the N−H and C═O groups, as shown in Figure 1. Specifically,

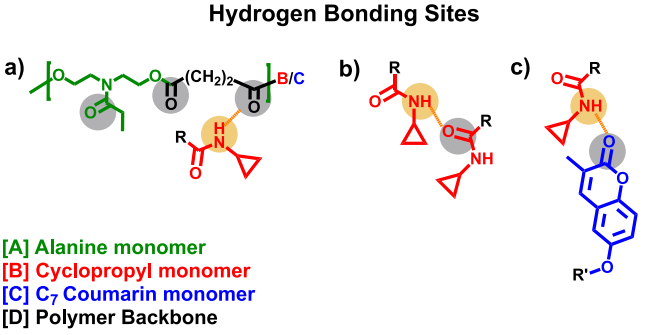

Figure 1. Chemical structure and proposed hydrogen bonding sites of [**A**], [**B**], and [**C**] in the polyesters $\mathbf{P_1}$, $\mathbf{P_2}$, $\mathbf{P_3}$, $\mathbf{P_4}$, and $\mathbf{P_5}$.

we focused on the absorption band around 3378 cm^{-1} (**band 2**) and the absorption band around 1750 cm^{-1} (**band 5**). **Band 2** was assigned to the N−H stretching vibration due to hydrogen bonding with the secondary amide group in monomer [**B**].[65,66] We observed a shift in this band from a low wavenumber to a high wavenumber as the temperature increased. This shift is attributed to the weakening of hydrogen bonding at higher temperatures, leading to the strengthening of the N−H bond.[67−69] **Band 5**, on the other hand, represents the unbonded C═O stretching vibration (1600−1900 cm^{-1}) associated with carbonyl groups from the ester group in the polymer backbone.[69] Interestingly, this appeared as a sharp band for $\mathbf{P_1}$ and $\mathbf{P_5}$, but it exhibited broadening for $\mathbf{P_3}$ and $\mathbf{P_4}$. This suggests the presence of physical cross-linking through hydrogen bonding interactions in the presence of both monomers [**B**] and [**C**]. However, no noticeable shift toward lower wavenumbers was observed for $\mathbf{P_3}$ and $\mathbf{P_4}$.

The absorption band at 1650 cm^{-1} (**band 6**) corresponds to the bonded C═O stretching frequency in the amide I mode, originating from the carboxyl group on the tertiary amide in the polymer backbone. We observed a shift in **band 6** for $\mathbf{P_1}$, $\mathbf{P_4}$, and $\mathbf{P_5}$ from a low wavenumber to a high wavenumber as

https://doi.org/10.1021/acs.biomac.3c00684
Biomacromolecules 2023, 24, 5091−5104

the temperature increased. This shift is indicative of weakening of the hydrogen bonding at higher temperatures and, consequently, strengthening of the C═O bond.[65,66,68] However, no apparent shift was observed for P_2 and P_3. Interestingly, we observed a split in **band 6**, resulting in **bands 6** and 7, as the monomer [**B**] concentration decreased and the monomer [**C**] concentration increased. This split can be attributed to the presence of both amide and ester groups. The shift of **band 7** for P_2 with increasing temperatures is due to weakening of the hydrogen bonding at high temperatures and thus C═O bond strengthening. However, the shift from high wavenumber to low wavenumber of **band 7** for P_4 and P_5 suggests increasing hydrogen bonding strength with increasing temperature. This increasing hydrogen bonding strength with increasing temperature suggests that the C═O from monomer [**C**] also contributes to physical cross-linking due to hydrogen bonding even at high temperatures.[65−6667] Finally, the absorption **band 8** was assigned to the amide II mode at 1550 cm^{-1}, which corresponds to the combination of the N−H bending and C−N stretching vibrations of the amide bond.[69] The shift of this band from high wavenumber to low wavenumber for P_1 and P_2 suggests increasing hydrogen bonding strength with increasing temperature. Interestingly, similar to **band 6**, there is also a split of **band 8** with decreasing monomer [**B**] concentration and increasing monomer [**C**] concentration. This split in this band may indicate different degrees of hydrogen bonding between adjacent amide groups from monomer [**C**] (Figure 2).

Overall, these studies reveal that all compositions exhibit a certain degree of water absorption, indicating the occurrence of hydrogen bonding even in the absence of the physical cross-linker monomer [**B**]. Compositions containing the physical cross-linker demonstrated stronger N−H stretching bands and hydrogen-bonded C═O vibrations compared to those without. Broader hydrogen-bonded vibrations (3363 cm^{-1}) were observed for compositions P_1−P_3 due to higher mol % amide groups. Interestingly, P_2 exhibited higher amide I intensities (1650 cm^{-1}) than P_1, suggesting stronger hydrogen bonding in the presence of the chemical cross-linker monomer [**C**]. Moreover, P_5 displayed relatively strong C═O vibrations (1600 cm^{-1}) suggesting that, in addition to the carbonyl group from the amide-containing [**B**] monomer, additional carbonyl groups on the pendant chains, the backbone of the polyesters, and the coumarin group in [**C**] monomer can likely provide extra hydrogen bonding sites. To confirm hydrogen bonding sites, molecular dynamics simulations were performed in the presence and absence of water.

3.4. Molecular Dynamics Simulations. From the VT-FTIR data, a high degree of hydrogen bonding that correlates with an increase in mol % of [**B**] was observed. Moreover, [**C**] exhibited a relatively high hydrogen bonding upon its incorporation into the polymer structure. Molecular dynamics simulations were employed to thoroughly characterize the hydrogen bonding sites at different polymer compositions. Simulations of polymer chains were conducted for both the dry polymers and for the systems with a minimal degree of water adsorption (<1 wt %). This methodological approach provides additional understanding about the nuanced effects of moisture on these polymers. Further simulation details and the corresponding methodology can be found in the Supporting Information.

Figure 3 exhibits the quantification of hydrogen bonds formed between polymer−polymer and polymer−water alongside a visual representation of the chemical structure of the functional groups involved. The hydrogen bonding between polymer chains happens in the presence of the NH functional group in [**B**] as P_5 molecules are absent of such polymer−polymer hydrogen bonding. In Figure 3a, the number of interchain hydrogen bonds between the NH functional groups in [**B**], the carbonyl oxygen of hydrophilic functional groups in [**A**], [**B**], and [**C**], and the backbone is shown in the absence of water molecules. The number of hydrogen bonds is time-averaged and normalized by the number of hydrophilic

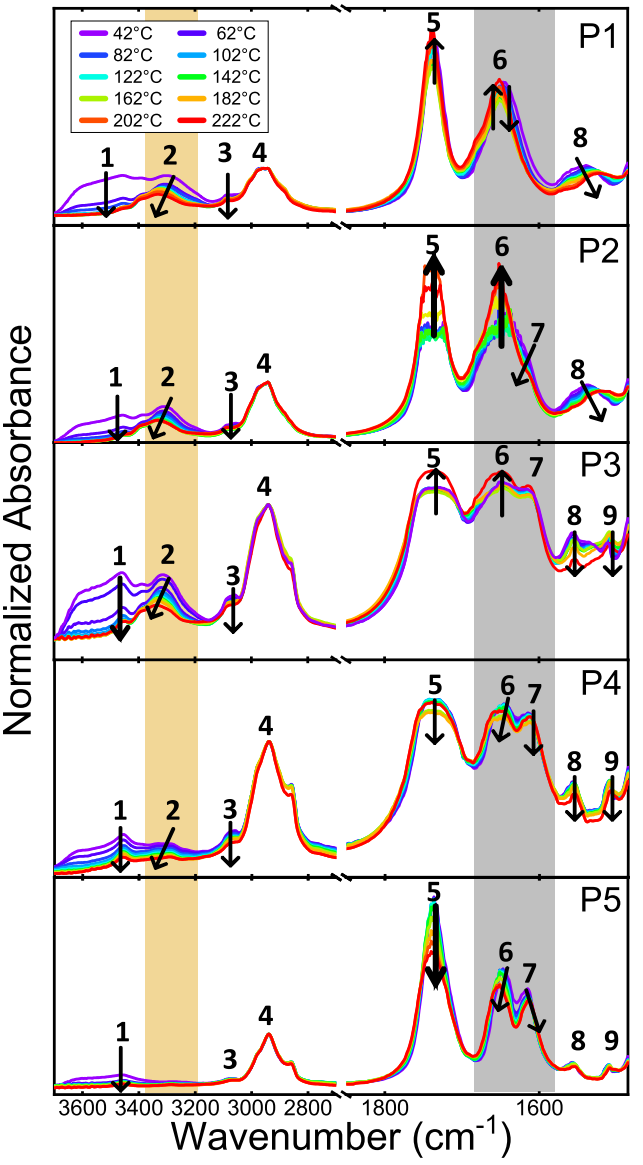

Figure 2. Temperature-dependent FT-IR spectra for: P_1, P_2, P_3, P_4, and P_5. Band description: (1) O−H stretching vibration from residual water (3500−3800 cm^{-1}),[64] (2) N−H stretching due to associated N−H stretching with the shift to a higher wavenumber due to hydrogen bonding weakening with increasing temperature (3363 cm^{-1}),[65,66,68] (3) C−H aromatic stretching (3066 cm-1), (4) C−H stretching (2964 cm^{-1}), (5) nonconjugated C═O stretching vibration from the ester group (1600−1900 cm^{-1}),[69] (6) hydrogen-bonded C═O stretching from amide I mode (1650 cm^{-1}) with major contribution from the backbone, (7) C═O stretching from amide I mode (1600 cm^{-1}) with major contribution from monomer [**C**],[65−6667] and (8−9) amide II mode from C−N stretching with N−H bending (1500−1600 cm^{-1}).[65−6667,69]

https://doi.org/10.1021/acs.biomac.3c00684
Biomacromolecules 2023, 24, 5091−5104

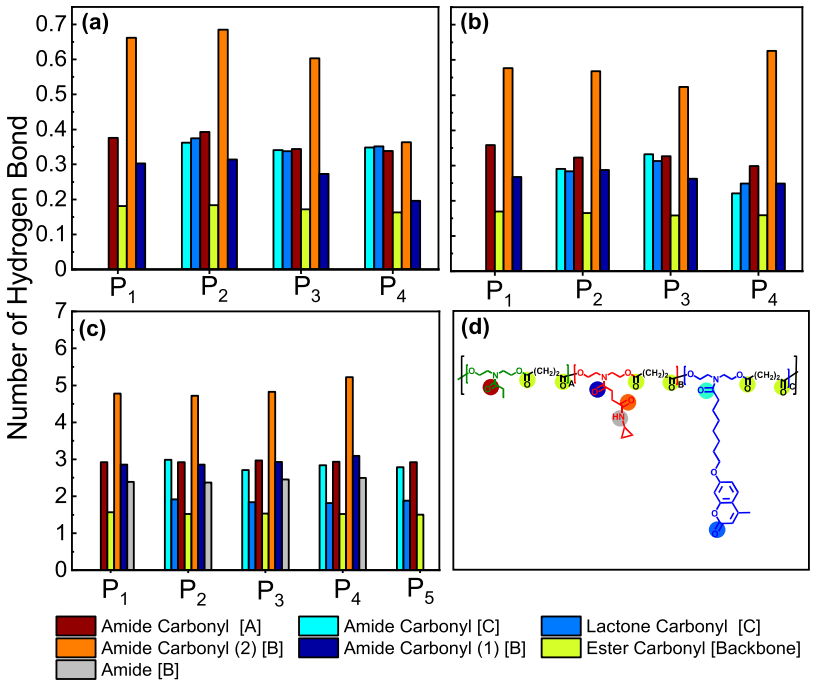

Figure 3. (a) Number of hydrogen bonds between polymer functional groups and NH in [**B**] for dry samples. The numbers are normalized by the corresponding number of functional groups and NH groups in each chain. (b) Number of hydrogen bonds between polymer functional groups and NH in [**B**] for samples with water adsorption. (c) Number of hydrogen bonds between polymer functional groups and water. The numbers were normalized by the corresponding number of functional groups in each chain. (d) Schematic of polymer functional groups in [**A**], [**B**], [**C**], and the backbone.

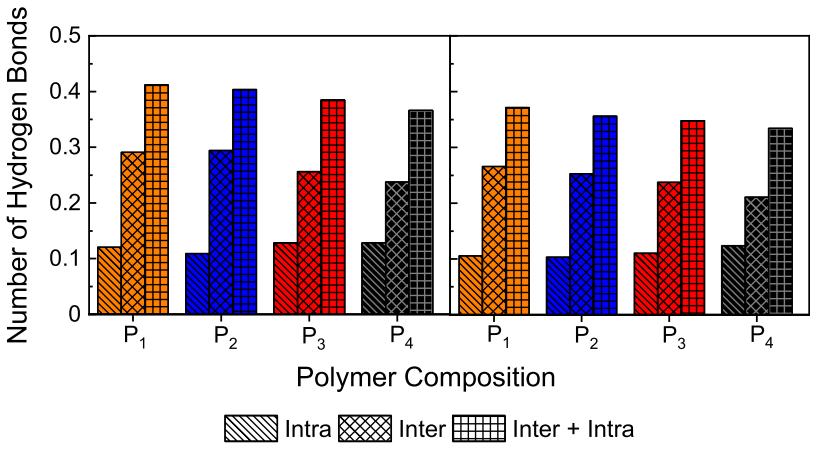

Figure 4. (a) Intra, inter, and total number of hydrogen bonds between polymer chains in the dry system. (b) Intra, inter, and total number of hydrogen bonds between polymer chains in the presence of water. The numbers are normalized by the corresponding number of functional groups in each chain.

functional groups and NH groups present in each chain, which leads to having numbers smaller than unity. This normalization allows for a clearer understanding of the contribution of each functional group to hydrogen bonding regardless of its concentration in the chain. It is evident that polymers with a higher number of [**B**] units have more total hydrogen bonding. From Figure 3a, it is seen that carbonyl oxygen of amide (2) in [**B**] contributes the most in interchain hydrogen bonding when compared to the other functional groups. The other primary sites, albeit with fewer hydrogen bonds, include the oxygen of the amide in [**A**] and [**C**] and the carbonyl oxygen of the ester in [**C**]. The carbonyl oxygen of amide (1) in [**B**] has fewer hydrogen bonds, while the carbonyl oxygen of esters in the backbone is the site with the least hydrogen bond number per chain. Furthermore, it is observed that by decreasing [**B**] units in the chain, the hydrogen bond numbers exhibit a decrease for both functional groups of amides in [**B**]. The remaining functional groups, however, display minimal fluctuations or remain mostly unchanged when the concentration of [**B**] or [**C**] is adjusted.

Figure 3b shows the number of hydrogen bonds of different functional groups in the presence of water. The data illustrate that the carbonyl oxygen of amide (2) in [**B**] is the primary site of interchain hydrogen bonding. Contrary to the system devoid of water molecules, $\mathbf{P_4}$ exhibits the highest level of hydrogen bonding for carbonyl amide (2) in [**B**], while $\mathbf{P_3}$ records the lowest value of hydrogen bonding for the corresponding functional group. For dry polymers, $\mathbf{P_2}$ displays the highest

https://doi.org/10.1021/acs.biomac.3c00684
Biomacromolecules 2023, 24, 5091−5104

Table 2. Binding Energy for P_1−P_5 with/without Water, where the Energy Unit is kcal·mol^{-1}

	polymer−polymer				
	without water		with water		
	inter	intra	inter	intra	polymer−water
P_1	−1388.2 ± 2.3	−652.6 ± 2.6	−1351.7 ± 3.4	−658.7 ± 3.6	−27.09 ± 0.49
P_2	−1383.5 ± 2.9	−631.9 ± 3.2	−1350.6 ± 2.0	−638.3 ± 2.4	−26.26 ± 0.86
P_3	−1379.9 ± 2.9	−592.0 ± 3.3	−1342.5 ± 2.0	−599.4 ± 2.4	−25.14 ± 0.83
P_4	−1374.4 ± 2.4	−555.3 ± 2.8	−1394.3 ± 2.7	−550.9 ± 3.0	−24.03 ± 0.79
P_5	−1369.2 ± 3.1	−536.7 ± 3.5	−1391.8 ± 2.8	−530.3 ± 3.2	−23.12 ± 0.79

count of hydrogen bonds for functional groups with [C]. The presence of water, however, alters this pattern, resulting in P_3 exhibiting a greater number of hydrogen bonds for functional groups in the [C] unit.

The number of hydrogen bonds between the polymer functional groups and water is shown in Figure 3c, where the hydrogen bond numbers are normalized by the number of corresponding functional groups in the chain. The carbonyl amide (2) group in [B] is the primary site of water adsorption and it is followed by the amides in [B], [C], and [A]. The carbonyl oxygen of the lactone in [C] displays less hydrogen bonding number, while the backbone ester exhibits the least number of hydrogen bonding with water.

The actual number of hydrogen bonds between the polymer chains for two systems (with and without water) are shown in Figure 4a,4b, dissected into intra- and interhydrogen bonding numbers. Decreasing [B] units leads to a reduction in total and interchain hydrogen bonding while a slight increase in intrachain hydrogen bonding is observed. The presence of water decreases the number of hydrogen bonding while the trend remains unchanged.

The normalized binding energy between hydrogen of NH in [B] with carbonyl oxygen of the functional groups for the dry system is shown in Figure S3.1a. The energy values are normalized by the number of corresponding functional groups and [B] units in the chain. The more negative values show a stronger binding energy between the pair of atoms. The figure shows that carbonyl amide oxygen in [A], [B], and [C] have a stronger binding energy when compared to the lactone carbonyl in [C] and carbonyl ester in the backbone. Moreover, the binding energy decreases with reducing the number of [B] units in the chain, which applies to both amide and ester functional groups. The binding energy of the system in the presence of water when compared to dry polymers follows the same trend, while the binding energy is weaker, as shown in Figure S3.1b. The binding energy of polymer−water is shown in Figure S3.1c, where the energy values are normalized by the number of functional groups in the chain. The binding energy associated with the amide and ester groups in [C] displays an inverse relationship with respect to the concentration of [C]. Herein, the most robust binding energy is observed for polymer P_2. Considering only the functional groups present in [B], which include amide groups and NH, the maximum binding energies are recorded at the lowest [B] concentration found in polymer P_4. Conversely, the weakest binding interaction with water is attributed to polymer P_2.

To gain a deeper understanding of the effects of water, calculations were performed to extract the binding energy for the polymer−polymer and water−polymer structures shown in Table 2. The calculation was carried out between the whole atoms of a chain with itself for intra-case and another chain for inter-case while prior binding energy values were between specific atoms of polymer or water. Regarding the binding energy between water and the polymer, normalized by the number of chains in the simulation box, there is an observable decrease in the strength of interaction as the proportion of [C] units increases within the polymer. Thus, one can infer that polymer P_1, without [C] units, exhibits a stronger hydrophilic character, while polymer P_5, with the highest concentration of [C] units, exhibits enhanced hydrophobic properties.

The intermolecular energies governing polymer−polymer interactions in the dry state are strongly correlated to the abundance of [C] units present within the polymer structure. Both polymers P_4 and P_5, which have higher concentrations of [C] units, exhibit the highest interchain binding energies, while their intrachain interactions are notably attenuated. Upon the introduction of water into the system, a distinct shift in the intermolecular interactions is observed. Specifically, polymers P_4 and P_5 display decreased interchain binding energies, while polymers P_1−P_3 exhibit enhanced interactions between chains. Furthermore, the adsorption of water appears to restructure the intrapolymeric configurations. Polymers P_4 and P_5 show increased intrachain binding energies, suggesting a greater degree of internal cohesion as the number of intrachain hydrogen bonding showed an increase, as shown in Figure 4b. Conversely, the intrachain interactions within polymers P_1−P_3 become comparatively weakened upon water uptake.

To summarize the outcomes of the simulation results, it is evident that the amide (2) group in [B] plays a pivotal role in facilitating hydrogen bonding between polymer chains. Additionally, this functional group serves as the primary site for water adsorption. The binding energy of the NH group in the [B] unit with the amide functional group is observed to be stronger when compared to its ester counterpart. Analysis of the water−polymer interaction energy reveals that the presence of [C] units amplify the hydrophobic nature of the polymer, while [B] units enhance the hydrophilic characteristics. Water uptake has differential effects on these polymers, depending on their hydrophilic or hydrophobic tendencies. For hydrophilic polymers (P_1−P_3), the presence of water boosts interchain interactions while simultaneously weakening intramolecular interactions. Conversely, for the more hydrophobic polymers (P_4 and P_5), water results in the intensification of intramolecular interactions. There is a competition between hydrophobic interactions for polymers with higher [C] monomers and hydrogen bonding interactions for those with more [B]. Moreover, polymers with more [B] form stronger binding energy with water, while removing water molecules in [C] dominant polymers (P_4 and P_5) has less binding energy. In addition, the presence of both hydrogen bonds and hydrophobic interactions will help the chains to facilitate intermolecular interactions where P_2−P_4 molecules are expected to exhibit a better performance for 3D printing applications.

https://doi.org/10.1021/acs.biomac.3c00684
Biomacromolecules 2023, 24, 5091−5104

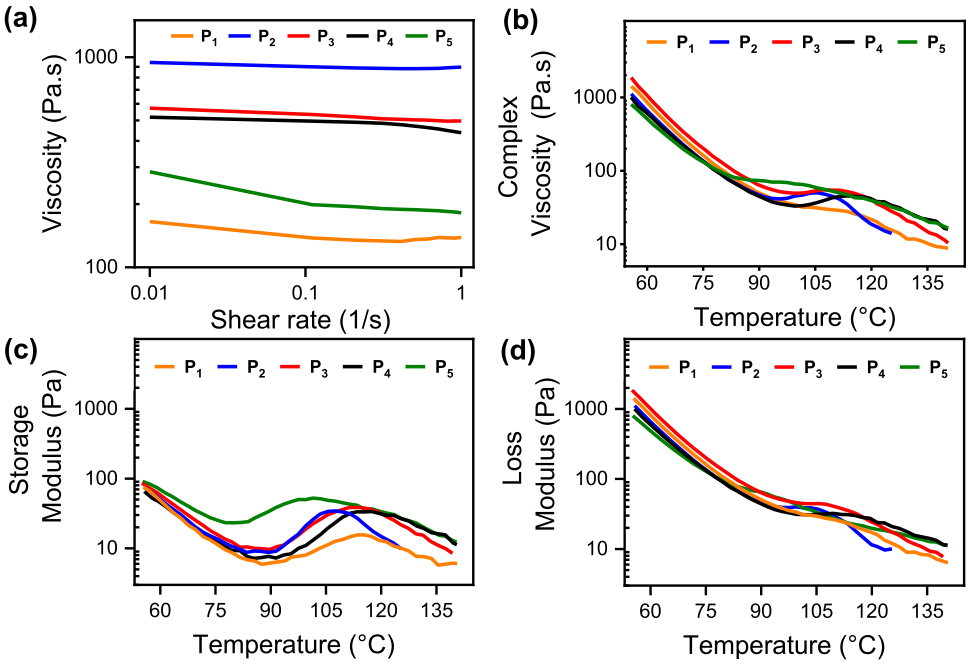

Figure 5. (a) Zero-shear viscosity as a function of shear rate at 65 °C for $\mathbf{P_1}$−$\mathbf{P_5}$, (b) complex viscosity as a function of temperature for $\mathbf{P_1}$−$\mathbf{P_5}$, and (c, d) temperature sweep of $\mathbf{P_1}$−$\mathbf{P_5}$ showing G' and G'' respectively.

3.5. Effect of Physical Cross-Linking on the Rheological Properties. To enable 3D printing of low-modulus polymers, they need to flow and exhibit shear thinning to ensure consistent extrusion. In order to ensure print fidelity, the polymers need to have sufficient zero-shear viscosity.[70,71] The zero-shear viscosity values (η_0) of the polymers (Table 1 and Figure 5a) suggest that if the polymers have only [**B**] or [**C**] ($\mathbf{P_1}$ and $\mathbf{P_5}$), there are insufficient physical cross-links (low η_0), resulting in a weak structure. However, when both [**B**] and [**C**] are present, this creates sufficient interactions between the polymer chains to provide resistance to flow (increased η_0). Note that the values of η_0 are prior to chemical cross-linking provided by [**C**]. $\mathbf{P_2}$ showed the highest viscosity, even though $\mathbf{P_1}$ has a higher amount of the hydrogen-bonding monomer [**B**]. These results indicate the possible existence of physical interactions involving monomer [**B**], the polymer backbone, and monomer [**C**]. Specifically, hydrogen bonding interactions between the NH groups of monomers [**B**] and the C═O group on the polymer backbone and monomer [**C**] are hypothesized. To study such interactions, further characterization with molecular dynamics and VT-FTIR was performed. The molecular dynamics simulations and the analysis of the binding energies (Figure S3.1) confirmed the hypothesized interactions between functional groups and the hydrogen bonding and hydrophobic interactions. The role of the water content adsorbed by the polymer was also identified as potentially critical in this context. In addition, VT-FTIR further ascertained these hydrogen bond interactions by the observed bands at 1650 and 1600 cm^{-1}. It is worth mentioning that many factors including interaction coefficients and the width of the polymer chain are contributing to zero-shear viscosity.[72,73] To decouple the effect of each pendant group from the viscosity, further in-depth characterization is needed, which will be the focus of future studies.

The shear thinning, zero-shear viscosity (η_0), and the effect of temperature and angular frequency on modulus were studied to understand the effects of these properties on shape fidelity. As determined by the steady-state response of viscosity (Figure 5a), only $\mathbf{P_4}$ and $\mathbf{P_5}$ showed shear-thinning behavior. This suggests that in $\mathbf{P_1}$−$\mathbf{P_3}$, the high concentration of [**B**] in the presence of [**C**] decreases polymer flow in the range of shear rates and temperatures examined. Higher temperatures and/or higher pneumatic pressure will be needed to ensure shear thinning for these polymers. Based on these results, we can confidently assert that all of the polymers investigated in this work hold potential as 3D printing inks. It is noteworthy that extrusion-based direct writing inks exhibit viscosities ranging from 30 mPa·s to 60 kPa·s, and our polymers fall within the desirable viscosity range.[11,74]

Figure 5c,d shows the variation of the storage modulus (G') and loss modulus (G'') with temperature. Between 80 and 85 °C, the modulus reaches a minimum for all polymers, and interestingly at ∼90 °C, there is a sudden modulus increase for all polymers. This increase in maxima is hypothesized to be a result of evaporation of trapped water molecules within the polymer chains at very high temperatures. The polymer overcomes the loss of water interactions by further enhancing polymer chain interactions. This hypothesis is supported by the results of the molecular dynamics simulations on intrapolymer and interpolymer interactions in wet and dry systems shown in Figures 3, 4, and S3.1 and Table 2. This increase in modulus at temperatures >90 °C coincides with the increase of the VT-FTIR band at ∼1650 cm^{-1} at temperatures between 182 and 202 °C (Figure 2) and suggests molecular chain rearrangements due to strong physical cross-linking. Famá et al. observed similar modulus behavior with increasing temperatures in a carbon nanotube−starch composite system, which induced significant change in the material elastic behavior.[75] From these results, we conclude that for $\mathbf{P_2}$, $\mathbf{P_3}$, and $\mathbf{P_4}$ systems, the hydrogen bonding [**B**] component induces stronger interactions between chains when combined with the unactivated chemical cross-linker group, thereby increasing the mechanical properties of the systems. In addition, from the temperature sweep experiments, we hypothesized printing

https://doi.org/10.1021/acs.biomac.3c00684
Biomacromolecules 2023, 24, 5091−5104

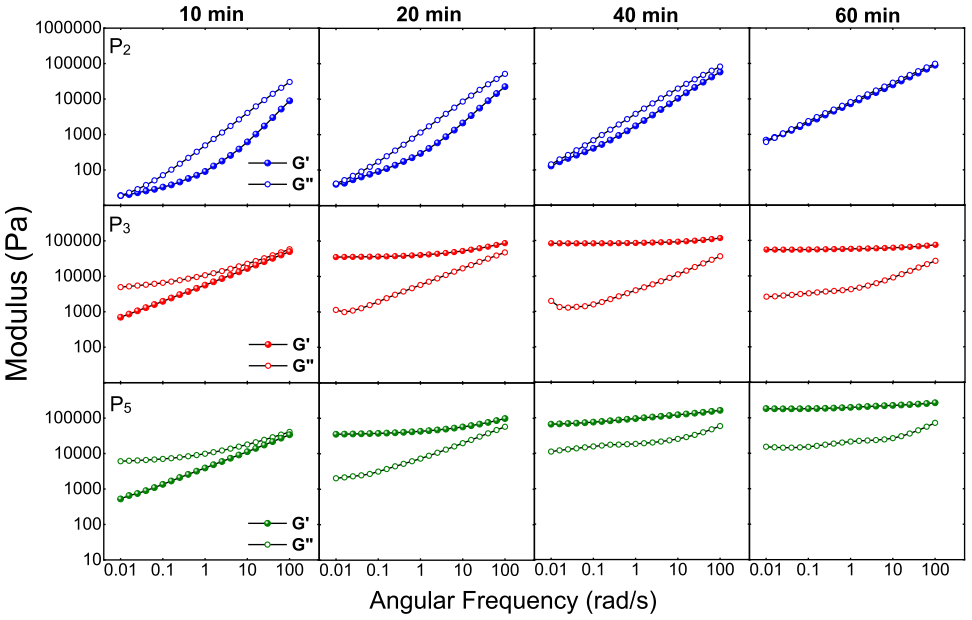

Figure 6. Small oscillation amplitude results at a reference temperature of 60 °C for (a) $\mathbf{P}_2$ and 65 °C for (b) $\mathbf{P}_3$ and (c) $\mathbf{P}_5$ after UV cross-linking.

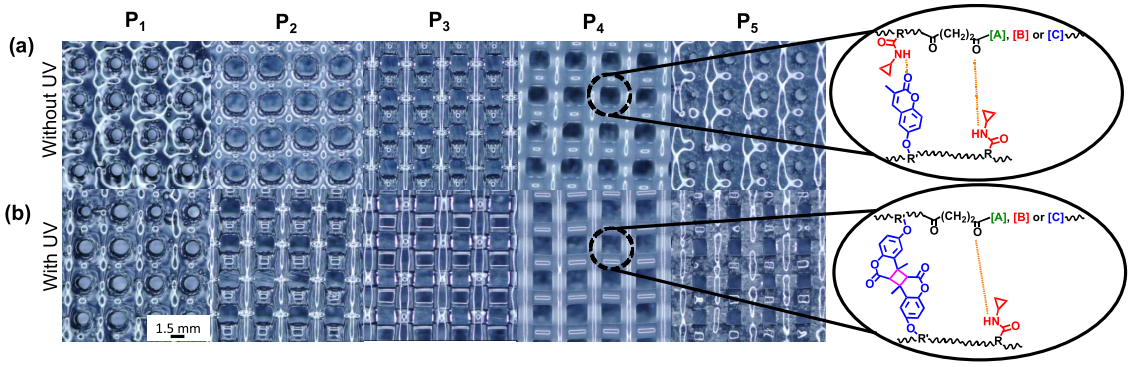

Figure 7. Study of shape fidelity by tracking the 3D printed scaffold pore shape change after 1 h in the presence of (a) physical cross-linkers only, provided by hydrogen bonding and (b) physical and chemical cross-linkers, provided by hydrogen bonding and by the [2 + 2] cycloaddition reaction of the C_7 coumarin monomer, respectively.

temperatures to be between 45 and 80 °C since all polymers showed modulus ≤100 Pa, which we have observed in our systems to be an optimal range for extrusion-based printing.[63] However, the printing pressure and temperature were confirmed by printing calibration experiments, as described in Section 3.7 and Figure S7.

3.6. Effect of Physical and Chemical Cross-Linking on Rheological Properties. Figures 6 and S4 show the small amplitude oscillatory shear measurements (SAOS) of $\mathbf{P}_2$, $\mathbf{P}_3$, and $\mathbf{P}_5$ with increasing UV cross-linking time. The gelation time for $\mathbf{P}_2$ occurs at 60 min, while for $\mathbf{P}_3$ and $\mathbf{P}_5$, the gelation time occurs at 10 min. G' increases quickly for $\mathbf{P}_3$ and $\mathbf{P}_5$ and exceeds G'' until G' reaches a plateau, while G'' gets close to a plateau, showing the formation of an elastic network. This data suggests that the molar ratio of physical and chemical cross-linkers is sufficient to convert the viscous polymer to the rubbery state. Interestingly, similar modulus is seen for $\mathbf{P}_3$ and $\mathbf{P}_5$ with increasing radiation time, even when $\mathbf{P}_3$ has only 20% of chemical cross-linkers while $\mathbf{P}_5$ has 40%. This means that in the presence of the physical cross-linker, the chemical cross-linker concentration can be lowered, and the polymer inks will have sufficient mechanical properties to obtain high shape fidelity. All five-polymer compositions were irradiated for the same time to maintain similar experimental conditions. Studies on the effect of physical and chemical cross-linkers on rheological and mechanical properties as well as swelling and degradation response are depicted in Figures S5 and S6.

3.7. 3D Printing and Shape Fidelity Assessment. Optimal print quality is greatly influenced by the printing temperature, pressure, and rate. To compare the respective roles of the physical [**B**] and chemical [**C**] cross-linkers, it is crucial to optimize these parameters. Consequently, different temperatures and pressures were evaluated to determine the best printing parameters. To ensure uniform mass among all printed scaffolds, we printed 2 mm long filaments at different printing pressures and temperatures. Specifically, we tested temperatures of 45, 55, and 65 °C, with the corresponding pressures of 100 to 300 kPa at intervals of 50 kPa. Figure S7 shows the speed at which the 2 mm filaments of each composition can be printed. It was found that the conditions that gave the optimum printing speed (<20 s per 2 mm) of the 2 mm filament was the temperature/pressure combination of 65 °C/150−250 kPa.

https://doi.org/10.1021/acs.biomac.3c00684
Biomacromolecules 2023, 24, 5091−5104

The 3D printability of the polyesters is based on their ability to satisfy circularity (C_r) and printability (P_r) parameters.[76] Circularity or $C_r = \frac{4\pi A}{P^2}$ is the undesired property of the extruded filament to fuse and deform, creating circular holes (where A is the area of the pore and P is the perimeter). Printability or $P_r = \frac{\pi}{4C_r}$ is the ability to form 3D structures with good fidelity and integrity (where C_r is circularity).[63,76] Systems with high shape fidelity show a uniform line width, $C_r < 1$ and $P_r = 1$, while systems with poor shape fidelity show a nonuniform line width, $C_r = 1$ and $P_r < 1$.

The shape fidelity of the 3D printed scaffolds was studied by comparing the pore shape change over time between non-cross-linked and cross-linked scaffolds and by calculating the Cr and Pr of cross-linked scaffolds after 1 h. Figure 7a shows that the physical cross-linker alone is not enough to provide good shape fidelity since pores collapse into a circular shape ($\mathbf{P_1}$). However, scaffolds with a combination of physical and chemical cross-linkers showed fewer circular pores, but still square pores (ideal geometry) were not observed. This was addressed by cross-linking the scaffolds to give an ideal pore shape (Figure 7b). $\mathbf{P_3}$ shows square pores and straight lines, while $\mathbf{P_4}$ and $\mathbf{P_5}$ show square pores but uneven and unaligned lines. Circularity and printability calculation results (Table 3 and Figure 8) quantitatively confirmed that a higher shape fidelity was observed in $\mathbf{P_3}$ systems, where the system showed the lowest C_r values and higher P_r values. This highlights that by substituting 20% of the chemical cross-linking group [**C**] with the physical cross-linking group [**B**], the shape fidelity can be enhanced.

Table 3. Printability and Circularity Values for Different 3D Printed Scaffold Compositions

polymer composition	circularity (C_r)	printability (P_r)
$\mathbf{P_1}$	0.977	0.808
$\mathbf{P_2}$	0.900	0.872
$\mathbf{P_3}$	0.840	0.935
$\mathbf{P_4}$	0.862	0.910
$\mathbf{P_5}$	0.872	0.900

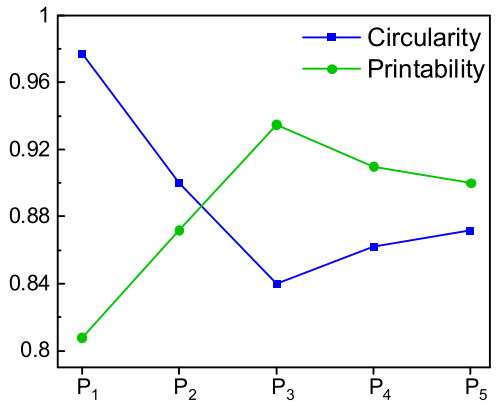

Figure 8. Printability and circularity results of different 3D printed scaffold compositions.

Next, we examined the use of composition $\mathbf{P_3}$ to create complex structures with overhanging features without the incorporation of any other additives or use of sacrificial inks. This polyester was used for 3D printing a human ear with a size of 34.55 mm × 32.05 mm × 8.70 mm, as shown in Figure 9. From these data, we confirm the excellent shape fidelity that $\mathbf{P_3}$ can provide. This polymer was used to print a complex structure at temperatures lower than 80 °C. It can also hold the shape of more than 50 layers and hanging lines while providing details from the design.

3.8. 3D Printed Scaffold In Vitro Cytotoxicity via Lactate Dehydrogenase (LDH) Activity Assay. To assess the biocompatibility of these materials, cytotoxicity was evaluated using the lactate dehydrogenase (LDH) assay with primary dermal fibroblasts; normal, human, and adult skin cells (HDFs). The LDH assay measures the leakage of the lactate dehydrogenase enzyme from damaged or dead cells with higher readings, indicating a larger proportion of the cell population being permeabilized.

The 3D printed scaffolds were incubated in media for 96 h to allow for degradation during which these scaffolds showed no evidence of morphological changes under light microscopy. This observation was supported by the LDH assay results as all scaffold supernatants exhibited low to minimal cytotoxicity, as shown in Figure 10, suggesting low concentrations of toxic degradation products. The materials that did show a relatively increased cytotoxicity over the course of 96 h, namely, $\mathbf{P_1}$ and $\mathbf{P_2}$, use a physical cross-linker concentration of 40 and 35% respectively, compared to the chemical cross-linker concentration in these polymers of 0 and 5% respectively, which suggests that the degradation rate controls these materials' cytotoxicity. Overall, these materials exhibited low cytotoxicity toward HDFs, suggesting their potential for use in tissue engineering scaffolds, optimizing the composition and ratio of physical and chemical cross-linkers to achieve both desired shape fidelity and biocompatibility.

4. CONCLUSIONS

The development of material systems for biomedical applications faces a significant challenge due to the limited availability of 3D printable systems with adequate biocompatibility. In this study, we address this challenge by designing five multifunctional polyester melts specifically tailored for solvent- and additive-free extrusion-based direct-write 3D printing. These polyesters possess different compositions of physical and chemical cross-linkers and are completely amorphous with T_g values of 13−16 °C.

By replacing 20% of the chemical cross-linking group [**C**] with the physical cross-linking group [**B**], the printable inks can improve shape fidelity without sacrificing the low-modulus nature of polymers. Furthermore, our temperature-dependent FT-IR absorption analysis revealed that hydrogen bonds acted as supramolecular cross-links, reinforcing the materials and restricting chain mobility at low temperatures. These observations were validated by molecular dynamics simulations that showed the roles of intra- and interchain hydrogen bonding in the polymers. These supramolecular interactions not only facilitated the shape retention ability of the 3D printed constructs but also improved their elastomeric-like properties. Rheological data showed a shift in temperature at the modulus maxima around ∼90 °C, suggesting further modulation of mechanical properties with temperature. Due to their low T_g, these polymers can be printed close to room temperature (45−65 °C) without solvents, diluents, or additives due to their relatively low viscosity. 3D printability analysis of these polyesters will assist in designing and

https://doi.org/10.1021/acs.biomac.3c00684
Biomacromolecules 2023, 24, 5091−5104

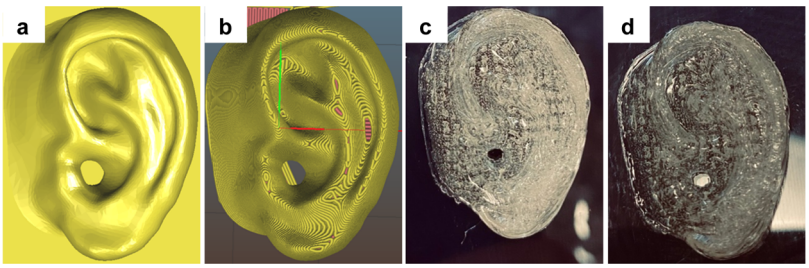

Figure 9. 3D printed human ear with a size of 34.55 × 32.05 × 8.70 mm^3 for shape fidelity studies. (a) Preview of the STL file, (b) Slic3r preview of the ear code, and (c, d) 3D printed ear with different lighting and magnification.

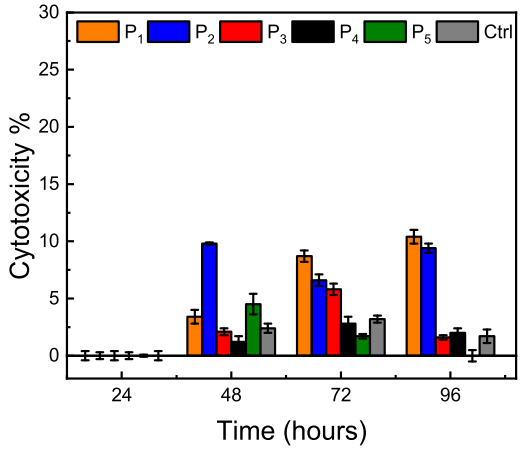

Figure 10. 3D printed scaffold cytotoxicity via lactate dehydrogenase (LDH) activity assay after scaffold degradation over 24, 48, 72, and 96 h.

developing 3D printable multifunctional polyesters with controlled physicochemical and mechanical properties. This work provides valuable insights into the interplay between hydrogen bonding and chain flexibility, demonstrating how altering the side-chain amide percentage and environmental conditions, such as temperature, can effectively modulate the polymer behavior.

■ ASSOCIATED CONTENT

Supporting Information

The Supporting Information is available free of charge at https://pubs.acs.org/doi/10.1021/acs.biomac.3c00684.

NMR characterization; rheological characterization; molecular dynamics simulations; swelling and degradation data; and 3D printing calibration (PDF)

■ AUTHOR INFORMATION

Corresponding Author

Abraham Joy − *School of Polymer Science and Polymer Engineering, The University of Akron, Akron, Ohio 44325, United States;* orcid.org/0000-0001-7781-3817; Email: abraham@uakron.edu

Authors

Deliris N. Ortiz-Ortiz − *School of Polymer Science and Polymer Engineering, The University of Akron, Akron, Ohio 44325, United States*

Abdol Hadi Mokarizadeh − *School of Polymer Science and Polymer Engineering, The University of Akron, Akron, Ohio 44325, United States;* orcid.org/0000-0001-5922-7654

Maddison Segal − *Department of Biomedical Engineering, The University of Akron, Akron, Ohio 44325, United States;* orcid.org/0009-0005-8404-7598

Francis Dang − *School of Polymer Science and Polymer Engineering, The University of Akron, Akron, Ohio 44325, United States*

Mahdi Zafari − *Department of Biology, The University of Akron, Akron, Ohio 44325, United States*

Mesfin Tsige − *School of Polymer Science and Polymer Engineering, The University of Akron, Akron, Ohio 44325, United States;* orcid.org/0000-0002-7540-2050

Complete contact information is available at: https://pubs.acs.org/10.1021/acs.biomac.3c00684

Notes

The authors declare no competing financial interest.

■ ACKNOWLEDGMENTS

This work was partially supported by funding from the NSF awards DMR 2114640 (to MT), DMR 2038515 (to AJ), and by the REU Site award at the University of Akron (DMR 2051052 (to MT/AJ)). We also acknowledge the helpful discussions about VT-FTIR data analysis with Dr. Steven Chuang and Aderinsola Oduntan.

■ REFERENCES

(1) Organ Donor List by the Health Resources & Service Administration. https://www.organdonor.gov/. (accessed September 28, 2023).

(2) Jung, J. W.; Lee, J. S.; Cho, D. W. Computer-Aided multiple-head 3D printing system for printing of heterogeneous organ/tissue constructs. *Sci. Rep.* **2016**, *6*, No. 21685, DOI: 10.1038/srep21685.

(3) Hockaday, L. A.; Kang, K. H.; Colangelo, N. W.; Cheung, P. Y. C.; Duan, B.; Malone, E.; Wu, J.; Girardi, L. N.; Bonassar, L. J.; Lipson, H.; Chu, C. C.; Butcher, J. T. Rapid 3D printing of anatomically accurate and mechanically heterogeneous aortic valve hydrogel scaffolds. *Biofabrication* **2012**, *4*, No. 035005, DOI: 10.1088/1758-5082/4/3/035005.

(4) Kang, H. W.; Lee, S. J.; Ko, I. K.; Kengla, C.; Yoo, J. J.; Atala, A. A 3D bioprinting system to produce human-scale tissue constructs with structural integrity. *Nat. Biotechnol.* **2016**, *34*, 312−319.

(5) Hinton, T. J.; Jallerat, Q.; Palchesko, R. N.; Park, J. H.; Grodzicki, M. S.; Shue, H. J.; Ramadan, M. H.; Hudson, A. R.; Feinberg, A. W. Three-dimensional printing of complex biological structures by freeform reversible embedding of suspended hydrogels. *Sci. Adv.* **2015**, *1*, No. 1500758.

(6) Jakus, A. E.; Rutz, A. L.; Jordan, S. W.; Kannan, A.; Mitchell, S. M.; Yun, C.; Koube, K. D.; Yoo, S. C.; Whiteley, H. E.; Richter, C. P.; Galiano, R. D.; Hsu, W. K.; Stock, S. R.; Hsu, E. L.; Shah, R. N. Hyperelastic 'bone': A highly versatile, growth factor-free, osteoregenerative, scalable, and surgically friendly biomaterial. *Sci. Transl. Med.* **2016**, *8*, No. 358ra127, DOI: 10.1126/scitranslmed.aaf7704.

(7) Kusaka, M.; Sugimoto, M.; Fukami, N.; Sasaki, H.; Takenaka, M.; Anraku, T.; Ito, T.; Kenmochi, T.; Shiroki, R.; Hoshinaga, K. Initial experience with a tailor-made simulation and navigation program using a 3-D printer model of kidney transplantation surgery. *Transplant. Proc.* **2015**, *47*, 596−599.
(8) Lee, J. W.; Choi, Y. J.; Yong, W. J.; Pati, F.; Shim, J. H.; Kang, K. S.; Kang, I. H.; Park, J.; Cho, D. W. Development of a 3D cell printed construct considering angiogenesis for liver tissue engineering. *Biofabrication* **2016**, *8*, No. 015007, DOI: 10.1088/1758-5090/8/1/015007.
(9) Yi, H. G.; Lee, H.; Cho, D. W. 3D printing of organs-on-chips. *Bioengineering* **2017**, *4*, No. 10, DOI: 10.3390/bioengineering4010010.
(10) Lee, J.-S.; Hong, J. M.; Jung, J. W.; Shim, J.-H.; Oh, J.-H.; Cho, D.-W. 3D printing of composite tissue with complex shape applied to ear regeneration. *Biofabrication* **2014**, *6*, No. 024103, DOI: 10.1088/1758-5082/6/2/024103.
(11) Ligon, S. C.; Liska, R.; Stampfl, J.; Gurr, M.; Mülhaupt, R. Polymers for 3D Printing and Customized Additive Manufacturing. *Chem. Rev.* **2017**, *117*, 10212−10290.
(12) Fina, F.; Goyanes, A.; Gaisford, S.; Basit, A. W. Selective laser sintering (SLS) 3D printing of medicines. *Int. J. Pharm.* **2017**, *529*, 285−293.
(13) Partee, B.; Hollister, S. J.; Das, S. Selective laser sintering process optimization for layered manufacturing of CAPA 6501 polycaprolactone bone tissue engineering scaffolds. *J. Manuf. Sci. Eng.* **2006**, *128*, 531−540.
(14) Lamichhane, S.; Bashyal, S.; Keum, T.; Noh, G.; Seo, J. E.; Bastola, R.; Choi, J.; Sohn, D. H.; Lee, S. Complex formulations, simple techniques: Can 3D printing technology be the Midas touch in pharmaceutical industry? *Asian J. Pharm. Sci.* **2019**, *14*, 465−479.
(15) Goyanes, A.; Buanz, A. B. M.; Basit, A. W.; Gaisford, S. Fused-filament 3D printing (3DP) for fabrication of tablets. *Int. J. Pharm.* **2014**, *476*, 88−92.
(16) Hospodiuk, M.; Dey, M.; Sosnoski, D.; Ozbolat, I. T. The bioink: A comprehensive review on bioprintable materials. *Biotechnol. Adv.* **2017**, *35*, 217−239.
(17) Allen, A. B.; Priddy, L. B.; Li, M. T. A.; Guldberg, R. E. Functional Augmentation of Naturally-Derived Materials for Tissue Regeneration. *Ann. Biomed. Eng.* **2015**, *43*, 555−567.
(18) Mano, J. F.; Silva, G. A.; Azevedo, H. S.; Malafaya, P. B.; Sousa, R. A.; Silva, S. S.; Boesel, L. F.; Oliveira, J. M.; Santos, T. C.; Marques, A. P.; Neves, N. M.; Reis, R. L. Natural origin biodegradable systems in tissue engineering and regenerative medicine: present status and some moving trends. *J. R. Soc. Interface* **2007**, *4*, 999−1030.
(19) Rindelaub, J. D.; Baird, Z.; Lindner, B. A.; Strantz, A. A. Identifying extractable profiles from 3D printed medical devices. *PLoS One* **2019**, *14*, No. e0217137.
(20) Morris, A. H.; Stamer, D. K.; Kyriakides, T. R. The host response to naturally-derived extracellular matrix biomaterials. *Semin. Immunol.* **2017**, *29*, 72−91.
(21) Nappier, K. M.; Smith, S.Toxicity of Common Extractables and Leachables of Medical Devices. In *Integrated Safety and Risk Assessment for Medical Devices and Combination Products*; Springer, 2019; Vol. *10*, pp 441−461.
(22) Schwab, A.; Levato, R.; D'Este, M.; Piluso, S.; Eglin, D.; Malda, J. Printability and Shape Fidelity of Bioinks in 3D Bioprinting. *Chem. Rev.* **2020**, *120*, 11028−11055.
(23) Zopf, D. A.; Hollister, S. J.; Nelson, M. E.; Ohye, R. G.; Green, G. E. Bioresorbable Airway Splint Created with a Three-Dimensional Printer. *N. Engl. J. Med.* **2013**, *368*, 2043−2045.
(24) Zhu, W.; Holmes, B.; Glazer, R. I.; Zhang, L. G. 3D printed nanocomposite matrix for the study of breast cancer bone metastasis. *Nanomed.: Nanotechnol. Biol. Med.* **2016**, *12*, 69−79.
(25) Chen, S. G.; Yang, J.; Jia, Y. G.; Lu, B.; Ren, L. TiO2 and PEEK Reinforced 3D Printing PMMA Composite Resin for Dental Denture Base Applications. *Nanomaterials* **2019**, *9*, No. 1049, DOI: 10.3390/nano9071049.
(26) Hong, S.; Sycks, D.; Chan, H. F.; Lin, S.; Lopez, G. P.; Guilak, F.; Leong, K. W.; Zhao, X. 3D Printing of Highly Stretchable and Tough Hydrogels into Complex, Cellularized Structures. *Adv. Mater.* **2015**, *27*, 4035−4040.
(27) Morrison, R. J.; Hollister, S. J.; Niedner, M. F.; Mahani, M. G.; Park, A. H.; Mehta, D. K.; Ohye, R. G.; Green, G. E. Mitigation of tracheobronchomalacia with 3D-printed personalized medical devices in pediatric patients. *Sci. Transl. Med.* **2015**, *7*, No. 285ra64.
(28) Zarek, M.; Mansour, N.; Shapira, S.; Cohn, D. 4D Printing of Shape Memory-Based Personalized Endoluminal Medical Devices. *Macromol. Rapid Commun.* **2017**, *38*, No. 1600628.
(29) Ma, H.; Suonan, A.; Zhou, J.; Yuan, Q.; Liu, L.; Zhao, X.; Lou, X.; Yang, C.; Li, D.; Zhang, Y. PEEK (Polyether-ether-ketone) and its composite materials in orthopedic implantation. *Arab. J. Chem.* **2021**, *14*, No. 102977.
(30) Deng, L.; Deng, Y.; Xie, K. AgNPs-decorated 3D printed PEEK implant for infection control and bone repair. *Colloids Surf., B* **2017**, *160*, 483−492.
(31) Sun, W.; Starly, B.; Daly, A. C.; Burdick, J. A.; Groll, J.; Skeldon, G.; Shu, W.; Sakai, Y.; Shinohara, M.; Nishikawa, M.; Jang, J.; Cho, D. W.; Nie, M.; Takeuchi, S.; Ostrovidov, S.; Khademhosseini, A.; Kamm, R. D.; Mironov, V.; Moroni, L.; Ozbolat, I. T. The bioprinting roadmap. *Biofabrication* **2020**, *12*, No. 022002.
(32) Jin, Z.; Li, Y.; Yu, K.; Liu, L.; Fu, J.; Yao, X.; Zhang, A.; He, Y. 3D Printing of Physical Organ Models: Recent Developments and Challenges. *Adv. Sci.* **2021**, *8*, No. 2101394.
(33) Sung, H. J.; Meredith, C.; Johnson, C.; Galis, Z. S. The effect of scaffold degradation rate on three-dimensional cell growth and angiogenesis. *Biomaterials* **2004**, *25*, 5735−5742.
(34) Kimura, A.; Aoki, M.; Fukushima, S.; Ishii, S.; Yamakoshi, K. Reconstruction of a defect of the rotator cuff with polytetrafluoroethylene felt graft: recovery of tensile strength and histocompatibility in an animal model. *J. Bone Jt. Surg., Br. Vol.* **2003**, *85*, 282−287, DOI: 10.1302/0301-620x.85b2.12823.
(35) Ozaki, J.; Fujimoto, S.; Masuhara, K.; Tamai, S.; Yoshimoto, S. Reconstruction of chronic massive rotator cuff tears with synthetic materials. *Clin. Orthop. Relat. Res.* **1986**, *202*, 173−183.
(36) Böstman, O. M.; Pihlajamäki, H. K. Adverse tissue reactions to bioabsorbable fixation devices. *Clin. Orthop. Relat. Res.* **2000**, *371*, 216−227.
(37) Liu, Y.; Ramanath, H. S.; Wang, D. A. Tendon tissue engineering using scaffold enhancing strategies. *Trends Biotechnol.* **2008**, *26*, 201−209.
(38) Karabay, U.; Husemoglu, R. B.; Egrilmez, M. Y.; Havitcioglu, H. A review of current developments in three-dimensional scaffolds for medical applications. *Turkish J. Plast. Surg.* **2021**, *29*, No. 38, DOI: 10.4103/tjps.tjps_70_20.
(39) Wang, H.; Xu, M.; Zhang, W.; Kwok, D. T. K.; Jiang, J.; Wu, Z.; Chu, P. K. Mechanical and biological characteristics of diamond-like carbon coated poly aryl-ether-ether-ketone. *Biomaterials* **2010**, *31*, 8181−8187.
(40) Gokhale, S.; Xu, Y.; Joy, A. A library of multifunctional polyesters with 'peptide-Like' pendant functional groups. *Biomacromolecules* **2013**, *14*, 2489−2493.
(41) Govindarajan, S. R.; Xu, Y.; Swanson, J. P.; Jain, T.; Lu, Y.; Choi, J. W.; Joy, A. A Solvent and Initiator Free, Low-Modulus, Degradable Polyester Platform with Modular Functionality for Ambient-Temperature 3D Printing. *Macromolecules* **2016**, *49*, 2429−2437.
(42) Govindarajan, S. R.; Jain, T.; Choi, J. W.; Joy, A.; Isayeva, I.; Vorvolakos, K. A hydrophilic coumarin-based polyester for ambient-temperature initiator-free 3D printing: Chemistry, rheology and interface formation. *Polymer* **2018**, *152*, 9−17.
(43) Swanson, J. P.; Cruz, M. A.; Monteleone, L. R.; Martinez, M. R.; Costanzo, P. J.; Joy, A. The effect of pendant group structure on the thermoresponsive properties of N -substituted polyesters. *Polym. Chem.* **2017**, *8*, 7195−7206.
(44) Nun, N.; Cruz, M.; Jain, T.; Tseng, Y. M.; Menefee, J.; Jatana, S.; Patil, P. S.; Leipzig, N. D.; McDonald, C.; Maytin, E.; Joy, A.

https://doi.org/10.1021/acs.biomac.3c00684
Biomacromolecules 2023, 24, 5091−5104

Thread Size and Polymer Composition of 3D Printed and Electrospun Wound Dressings Affect Wound Healing Outcomes in an Excisional Wound Rat Model. *Biomacromolecules* **2020**, *21*, 4030−4042.
(45) Jain, T.; Saylor, D.; Piard, C.; Liu, Q.; Patel, V.; Kaushal, R.; Choi, J. W.; Fisher, J.; Isayeva, I.; Joy, A. Effect of Dexamethasone on Room Temperature Three-Dimensional Printing, Rheology, and Degradation of a Low Modulus Polyester for Soft Tissue Engineering. *ACS Biomater. Sci. Eng.* **2019**, *5*, 846−858.
(46) Jain, T.; Tseng, Y. M.; Tantisuwanno, C.; Menefee, J.; Shahrokhian, A.; Isayeva, I.; Joy, A. Synthesis, Rheology, and Assessment of 3D Printability of Multifunctional Polyesters for Extrusion-Based Direct-Write 3D Printing. *ACS Appl. Polym. Mater.* **2021**, *3*, 6618−6631.
(47) Xu, Y.; Liu, Q.; Narayanan, A.; Jain, D.; Dhinojwala, A.; Joy, A. Mussel-Inspired Polyesters with Aliphatic Pendant Groups Demonstrate the Importance of Hydrophobicity in Underwater Adhesion. *Adv. Mater. Interfaces* **2017**, *4*, No. 1700506.
(48) Kaur, S.; Narayanan, A.; Dalvi, S.; Liu, Q.; Joy, A.; Dhinojwala, A. Direct Observation of the Interplay of Catechol Binding and Polymer Hydrophobicity in a Mussel-Inspired Elastomeric Adhesive. *ACS Cent. Sci.* **2018**, *4*, 1420−1429.
(49) Trimmer, B.; Lewis, J. A.; Shepherd, R. F.; Lipson, H. 3D Printing Soft Materials: What Is Possible? *Soft Rob.* **2015**, *2*, 3−6.
(50) Ribeiro, A.; Blokzijl, M. M.; Levato, R.; Visser, C. W.; Castilho, M.; Hennink, W. E.; Vermonden, T.; Malda, J. Assessing bioink shape fidelity to aid material development in 3D bioprinting. *Biofabrication* **2018**, *10*, No. 014102.
(51) Hart, L. R.; Li, S.; Sturgess, C.; Wildman, R.; Jones, J. R.; Hayes, W. 3D Printing of Biocompatible Supramolecular Polymers and their Composites. *ACS Appl. Mater. Interfaces* **2016**, *8*, 3115−3122.
(52) Wei, P.; Yan, X.; Cook, T. R.; Ji, X.; Stang, P. J.; Huang, F. Supramolecular Copolymer Constructed by Hierarchical Self-Assembly of Orthogonal Host-Guest, H-Bonding, and Coordination Interactions. *ACS Macro Lett.* **2016**, *5*, 671−675.
(53) Lu, Y. S.; Yu, C. Y.; Lin, Y. C.; Kuo, S. W. Hydrogen bonding strength of diblock copolymers affects the self-assembled structures with octa-functionalized phenol POSS nanoparticles. *Soft Matter* **2016**, *12*, 2288−2300.
(54) Lübtow, M.; Helmers, I.; Stepanenko, V.; Albuquerque, R. Q.; Marder, T. B.; Fernández, G. Self-Assembly of 9,10-Bis-(phenylethynyl) Anthracene (BPEA) Derivatives: Influence of $\pi-\pi$ and Hydrogen-Bonding Interactions on Aggregate Morphology and Self-Assembly Mechanism. *Chem. - Eur. J.* **2017**, *23*, 6198−6205, DOI: 10.1002/chem.201605989.
(55) Chen, Y.; Guan, Z. Multivalent hydrogen bonding block copolymers self-assemble into strong and tough self-healing materials. *Chem. Commun.* **2014**, *50*, 10868−10870.
(56) Ahn, B. K.; Lee, D. W.; Israelachvili, J. N.; Waite, J. H. Surface-initiated self-healing of polymers in aqueous media. *Nat. Mater.* **2014**, *13*, 867−872.
(57) Roy, N.; Tomović, Ž.; Buhler, E.; Lehn, J. M. An Easily Accessible Self-Healing Transparent Film Based on a 2D Supramolecular Network of Hydrogen-Bonding Interactions between Polymeric Chains. *Chem. - Eur. J.* **2016**, *22*, 13513−13520, DOI: 10.1002/chem.201601378.
(58) Faghihnejad, A.; Feldman, K. E.; Yu, J.; Tirrell, M. V.; Israelachvili, J. N.; Hawker, C. J.; Kramer, E. J.; Zeng, H. Adhesion and Surface Interactions of a Self-Healing Polymer with Multiple Hydrogen-Bonding Groups. *Adv. Funct. Mater.* **2014**, *24*, 2322−2333.
(59) Ahn, B. K. Perspectives on Mussel-Inspired Wet Adhesion. *J. Am. Chem. Soc.* **2017**, *139*, 10166−10171.
(60) Jin, X.; Wang, W.; Xiao, C.; Lin, T.; Bian, L.; Hauser, P. Improvement of coating durability, interfacial adhesion and compressive strength of UHMWPE fiber/epoxy composites through plasma pre-treatment and polypyrrole coating. *Compos. Sci. Technol.* **2016**, *128*, 169−175.
(61) Aguilar, M. R.; Román, J. S. Introduction to Smart Polymers and Their Applications. In *Smart Polymers and Their Applications*; Woodhead Publishing, 2019; pp 1−11.
(62) McNair, O. D.; Brent, D. P.; Sparks, B. J.; Patton, D. L.; Savin, D. A. Sequential thiol click reactions: Formation of ternary thiourethane/thiol- ene networks with enhanced thermal and mechanical properties. *ACS Appl. Mater. Interfaces* **2014**, *6*, 6088−6097.
(63) Liu, Q.; Jain, T.; Peng, C.; Peng, F.; Narayanan, A.; Joy, A. Introduction of Hydrogen Bonds Improves the Shape Fidelity of Viscoelastic 3D Printed Scaffolds while Maintaining Their Low-Temperature Printability. *Macromolecules* **2020**, *53*, 3690−3699.
(64) Madejová, J.; Janek, M.; Komadel, P.; Herbert, H. J.; Moog, H. C. FTIR analyses of water in MX-80 bentonite compacted from high salinary salt solution systems. *Appl. Clay Sci.* **2002**, *20*, 255−271.
(65) Chen, X.; Zawaski, C. E.; Spiering, G. A.; Liu, B.; Orsino, C. M.; Moore, R. B.; Williams, C. B.; Long, T. E. Quadruple Hydrogen Bonding Supramolecular Elastomers for Melt Extrusion Additive Manufacturing. *ACS Appl. Mater. Interfaces* **2020**, *12*, 32006−32016.
(66) Chen, X.; Zhang, K.; Talley, S. J.; Orsino, C. M.; Moore, R. B.; Long, T. E. Quadruple hydrogen bonding containing supramolecular thermoplastic elastomers: Mechanical and morphological correlations. *J. Polym. Sci., Part A: Polym. Chem.* **2019**, *57*, 13−23.
(67) Skrovanek, D. J.; Howe, S. E.; Painter, P. C.; Coleman, M. M. Hydrogen Bonding in Polymers: Infrared Temperature Studies of an Amorphous Polyamide. *Macromolecules* **1985**, *18*, 1676−1683.
(68) Skrovanek, D. J.; Painter, P. C.; Coleman, M. M. Hydrogen Bonding in Polymers. 2. Infrared Temperature Studies of Nylon 11. *Macromolecules* **1986**, *19*, 699−705.
(69) Coleman, M. M.; Skrovanek, D. J.; Painter, P. C. Hydrogen bonding in polymers: III further infrared temperature studies of polyamides. *Makromol. Chem., Macromol. Symp.* **1986**, *5*, 21−33.
(70) Aho, J.; Boetker, J. P.; Baldursdottir, S.; Rantanen, J. Rheology as a tool for evaluation of melt processability of innovative dosage forms. *Int. J. Pharm.* **2015**, *494*, 623−642.
(71) Jones, N. Science in three dimensions: The print revolution. *Nature* **2012**, *487*, 22−23.
(72) Breitling, S. M.; Magill, J. H. A model for the Magill - Li viscosity - temperature relation. *J. Appl. Phys.* **1974**, *45*, 4167−4171.
(73) Privalko, V. P.; Lipatov, Y. S. The possibility of folding of macromolecules in amorphous polymers. Dependence of the molecular packing density and viscosity of polymer melts on molecular weight. *Polym. Sci. U.S.S.R.* **1976**, *18*, 1133−1140.
(74) Murphy, S. V.; Atala, A. 3D bioprinting of tissues and organs. *Nat. Biotechnol.* **2014**, *32*, 773−785.
(75) Famá, L.; Rojo, P. G.; Bernal, C.; Goyanes, S. Biodegradable starch based nanocomposites with low water vapor permeability and high storage modulus. *Carbohydr. Polym.* **2012**, *87*, 1989−1993.
(76) Ouyang, L.; Yao, R.; Zhao, Y.; Sun, W. Effect of bioink properties on printability and cell viability for 3D bioplotting of embryonic stem cells. *Biofabrication* **2016**, *8*, No. 035020.

https://doi.org/10.1021/acs.biomac.3c00684
Biomacromolecules 2023, 24, 5091−5104